Journal of Materials Chemistry C

ROYAL SOCIETY OF CHEMISTRY

PAPER

View Article Online
View Journal | View Issue

Open Access Article. Published on 10 March 2021. Downloaded on 8/24/2022 2:34:21 PM.
This article is licensed under a Creative Commons Attribution-NonCommercial 3.0 Unported Licence.

Check for updates

Cite this: J. Mater. Chem. C, 2021, 9, 4486

N-Doping improves charge transport and morphology in the organic non-fullerene acceptor O-IDTBR†

Alexandra F. Paterson,*[ab] Ruipeng Li,[c] Anastasia Markina,[d] Leonidas Tsetseris,[e] Sky MacPhee,[b] Hendrik Faber,[b] Abdul-Hamid Emwas,[f] Julianna Panidi,[g] Helen Bristow,[h] Andrew Wadsworth,[h] Derya Baran,[b] Denis Andrienko,[d] Martin Heeney,[g] Iain McCulloch[bh] and Thomas D. Anthopoulos*[b]

Received 14th December 2020,
Accepted 10th March 2021

DOI: 10.1039/d0tc05861k

rsc.li/materials-c

Molecular doping has been shown to improve the performance of various organic (opto)electronic devices. When compared to p-doped systems, research into n-doped organic small-molecules is relatively limited, primarily due to the lack of suitable dopants and the often encountered unfavourable microstructural effects. These factors have prevented the use of n-doping in a wider range of existing materials, such as non-fullerene acceptors (NFAs), that have already shown great promise for a range of (opto)electronic applications. Here, we show that several different molecular n-dopants, namely [1,2-*b*:2′,1′-*d*]benzo[*i*][2.5]benzodiazocine potassium triflate adduct (DMBI-BDZC), tetra-*n*-butylammonium fluoride (TBAF) and 4-(2,3-dihydro-1,3-dimethyl-1*H*-benzimidazol-2-yl)-*N*,*N*-dimethylbenzenamine (N-DMBI), can be used to n-dope the molecular semiconductor O-IDTBR, a promising NFA, and increase the electron field-effect mobility to >1 cm^2 V^{-1} s^{-1}. By combining complementary experimental techniques with computer simulations of doping and charge carrier dynamics, we show that improved charge transport arises from synergistic effects of n-type doping and morphological changes. Specifically, a new, previously unreported dopant-induced packing orientation results in one of the highest electron mobility values reported to-date for an NFA molecule. Overall, this work highlights the importance of dopant–semiconductor interactions and their impact on morphology, showing that dopant-induced molecular packing motifs may be generic and a key element of the charge transport enhancement observed in doped organics.

Introduction

Electronic doping is an established technique throughout the semiconductor industry. Specifically: carefully selecting and incorporating an additional material into a host semiconductor to induce (or remove) electrons allows for the accurate control of the charge transport in the semiconductor.[1–3] This, in turn, can have enormous impact on the key performance metrics in a broad range of electronic devices: from incumbent inorganic semiconductors to emergent organic semiconductors (OSCs), and their application in transistors, solar cells, photodetectors, and light emitting diodes. For example, in organic thin-film transistors (OTFTs), molecular doping has been shown to greatly improve all operating characteristics.[4,5]

Yet despite the clear evidence that doping has extreme beneficial qualities, to-date, there remain a few key categories of semiconductor that have been explored significantly less than others. For example, in OSCs, doping has been widely explored in hole transporting (p-type) polymers; on the other

[a] Department of Chemical and Materials Engineering, and Centre for Applied Energy Research, University of Kentucky, Lexington, Kentucky, 40506, USA. E-mail: alexandra.paterson@uky.edu
[b] King Abdullah University of Science and Technology, KAUST Solar Centre, Thuwal, 23955-6900, Saudi Arabia
[c] National Synchrotron Light Source II (NSLS II), Brookhaven National Lab, Upton, New York, USA
[d] Max Planck Institute for Polymer Research, Ackermannweg 10, 55128 Mainz, Germany
[e] Department of Physics, National Technical University of Athens, Athens GR-15780, Greece
[f] Core Labs, King Abdullah University of Science and Technology, Thuwal 23955-6900, Saudi Arabia
[g] Department of Chemistry and Centre for Plastic Electronics, Imperial College London, South Kensington, London SW7 2AZ, UK
[h] Department of Chemistry, Chemistry Research Laboratory, University of Oxford, Oxford OX1 3TA, UK

† Electronic supplementary information (ESI) available. See DOI: 10.1039/d0tc05861k

This journal is © The Royal Society of Chemistry 2021

Open Access Article. Published on 10 March 2021. Downloaded on 8/24/2022 2:34:21 PM.
This article is licensed under a Creative Commons Attribution-NonCommercial 3.0 Unported Licence.

hand, investigation into doped electron transporting (n-type) small-molecules remains scarce. Reasons for this include: (i) the requirement for extreme energetics that lead to unstable n-type dopants,[3] and (ii) low doping efficiencies due to limited solubility/miscibility.[2,6–8] The former makes it extremely difficult to identify materials that act as n-type dopants,[7] whereas the latter can result in structural defects with adverse effects on charge transport – especially in highly crystalline small-molecule OSCs.[6,9] This is particularly the case for solution-processed small-molecules: final layer-morphology is governed by complex interactions between processing conditions, such as solvent-drying kinetics, and nucleation and growth processes. The introduction of an additional component (dopant) and its coupling to the host semiconductor can significantly alter such mechanisms, thereby impacting the final layer microstructure.

However, recent studies suggest the presence of dopant molecules does not necessarily have a detrimental impact on OSC morphology. Indeed, Jacobs and Moulé noted that the strong coupling between solubility, doping and morphology could instead be exploited to pattern OSCs and control crystallinity.[2] This is further supported by the fact that Lewis acids, such as $B(C_6F_5)_3$ and $Zn(C_6F_5)_2$, have recently been shown to play the role of both molecular dopant and morphology modifiers.[10,11] Along with the steady growth in the library of n-type molecular dopants,[12–14] these latest observations are important for solution-processed n-type small-molecules – especially for those that have already shown to be exceptional OSCs for various applications. For example, materials such as non-fullerene acceptors (NFAs) have received great interest in recent years in the field of organic photovoltaics (OPVs). Their role in achieving record OPV efficiencies (>15%) arises from a number of inherent, desirable NFA-characteristics,[15] including synthetically tuneable optical properties, improved long-term morphological stability and high charge carrier mobility, μ.[16] In terms of the latter property, one such NFA, O-IDTBR, has shown a superior structure/packing motif as compared to other NFAs, leading to impressive $\mu_e \approx 0.12$ cm^2 V^{-1} s^{-1} measured in OTFTs.[17] If n-doping were to further enhance the charge transport of O-IDTBR, it would be of significant and broad interest to the organic electronics community, with relevance to solar cells, photodetectors and transistors.

Here, we use thin-film transistors and computer simulations of doping and charge dynamics, to investigate the impact of n-doping on the transport characteristics of solution-processed O-IDTBR. We use two relatively unexplored molecular n-type dopants, [1,2-*b*:2′,1′-*d*]benzo[*i*][2.5]benzodiazocine potassium triflate adduct (DMBI-BDZC) and tetra-*n*-butylammonium fluoride (TBAF), and one well-known molecular n-type dopant *N*,*N*-dimethylbenzenamine (N-DMBI). We find that one of the most striking effects from the simple, solution-phase admixing of each dopant, is the significant increase in electron mobility, reaching values in excess of 1 cm^2 V^{-1} s^{-1} with all n-dopants: the highest reported electron mobility for an NFA small-molecule to-date, and the first example of exploiting molecular doping for enhancing the carrier transport in NFA-based transistor. Electron paramagnetic resonance (EPR) spectroscopy and transistor measurements suggest the improvement in mobility arises from successful n-type doping, atomic force microscopy and grazing incidence wide-angle X-ray scattering suggest the dopants also act as additives that affect the layer morphology. Furthermore, microstructural analysis *via* X-ray diffraction (XRD) measurements uncovers a previously unidentified O-IDTBR orientation/packing motif, with preferential in-plane π-stacking, in the optimally doped systems. Theoretical analysis from density functional theory (DFT), molecular dynamics and kinetic Monte Carlo simulations, confirm the mobility improvement is the result of the synergistic n-type doping and morphology changes. Overall, we identify an important mechanism on dopant interactions and their impact on host-semiconductor morphology – where the latter is typically thought to be a key bottleneck to the widespread implementation of doping in organic semiconductors.

Results and discussion

Dopant and material identification

We began by selecting suitable molecular dopants for O-IDTBR (Fig. 1a). A historically limited choice of n-dopants is mainly because of difficulties in finding air-stable materials with ionization energies high enough to initiate electron transfer to the host-OSC LUMOs.[6,18] Despite these difficulties, we recently identified [1,2-*b*:2′,1′-*d*]benzo[*i*][2.5]benzodiazocine potassium triflate adduct (DMBI-BDZC) (Fig. 1d) as a suitable charge transfer n-dopant.[13] Other n-dopants – that utilise alternative doping mechanisms – have also been identified in the literature, with two exemplary materials being tetra-n-butylammonium fluoride (TBAF) (Fig. 1b),[12,19,20] and 4-(2,3-dihydro-1,3-dimethyl-1*H*-benzimidazol-2-yl)-*N*,*N*-dimethylbenzenamine (N-DMBI) (Fig. 1c).[14,21,22] To test the applicability of DMBI-BDZC, TBAF and N-DMBI as n-dopants in O-IDTBR, we studied each system using EPR. The latter technique can be used to detect whether free charge carriers have been generated in a system with the addition of a dopant;[23,24] if such fundamental exchange mechanisms exist between host and dopant, an increase in EPR signal is expected.[12,25] Fig. 1e shows EPR data for O-IDTBR solutions with TBAF, N-DMBI and DMBI-BDZC at highly doped molar percentages (10 mol%) of the total O-IDTBR molar mass. Whilst the EPR signal for pristine O-IDTBR remains flat, a strong increase in signal is observed with each dopant. Although the signal becomes more intense from DMBI-BDZC to N-DMBI and finally TBAF, the data indicates successful n-type doping of O-IDTBR with all dopants. In addition to this finding for O-IDTBR, these three materials have been shown to have positive effects in other OTFTs,[12,13,22] with unusual and original doping mechanisms that are still largely unknown. We therefore chose to focus our study on these n-dopant materials.

Organic thin-film transistors

Having identified appropriate n-dopants for O-IDTBR, we investigated their impact in the operating characteristics of

Open Access Article. Published on 10 March 2021. Downloaded on 8/24/2022 2:34:21 PM.
This article is licensed under a Creative Commons Attribution-NonCommercial 3.0 Unported Licence.

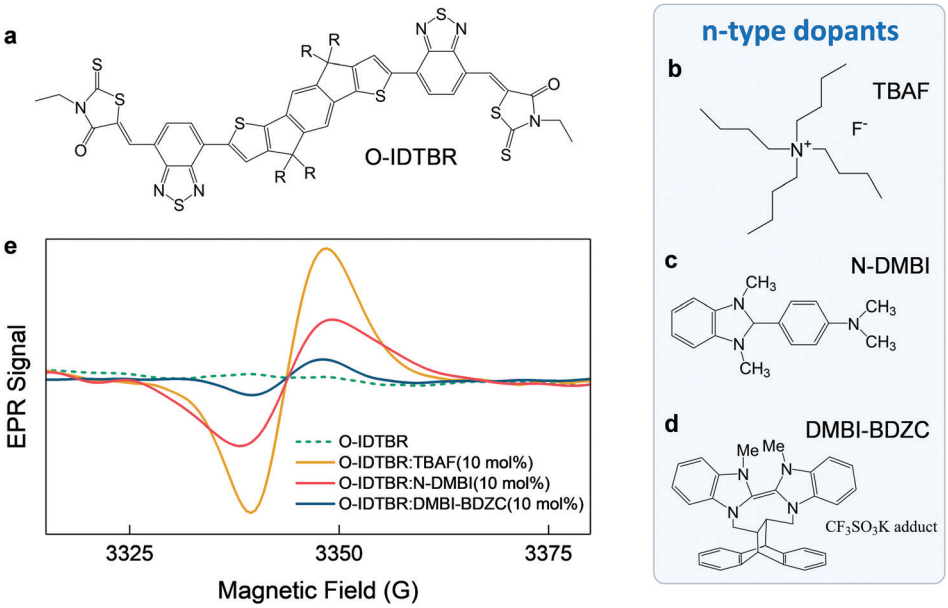

Fig. 1 Chemical structures for (a) O-IDTBR, (b) tetra-*n*-butylammonium fluoride (TBAF), (c) 4-(2,3-dihydro-1,3-dimethyl-1*H*-benzimidazol-2-yl)-*N*,*N*-dimethylbenzenamine (N-DMBI) and (d) [1,2-*b*:2′,1′-*d*]benzo[*i*][2.5]benzodiazocine potassium triflate adduct, $C_{34}H_{30}N_4$ (DMBI-BDZC). (e) Electron paramagnetic resonance data, showing each n-dopant generates free chare carriers in O-IDTBR.

O-IDTBR OTFTs. Transistors are known for being an excellent tool to investigating molecular dopants in semiconductors: specifically, the operation of OTFTs are highly sensitive to trap states and their distribution. A successful dopant will fill such trap states and reduce energetic disorder, which is subsequently characterised by the improvement of transistor operating characteristics, such as threshold voltage, subthreshold slope, mobility or bias-stress stability.[26] Top-gate, bottom-contact (TG-BC) architecture OTFTs were therefore fabricated at a broad range of doping concentrations, 0.001, 0.01, 0.1, 1 and 10 mol%, for each n-dopant. We chose a diverse range of dopant concentrations to probe the limitations of doping in this molecular system, namely: (i) the point at which electronic doping no longer improves the electron mobility of the OTFT and instead increases the bulk conductivity of the channel, and (ii) the intrinsic miscibility limit between the host OSC and the different dopants. Fig. 2a shows representative transfer curves at best-performing concentrations, which were found to be 1, 0.01 and 1 mol% for TBAF-, N-DMBI- and DMBI-BDZC-doped transistors, respectively. An overview of OTFT parameters and output curves are given in Table 1 and Fig. S1 (ESI†), respectively. We find that all best-performing transistors increase in drain current (I_D), and highly doped (10 mol%) TBAF and DMBI-BDZC OTFTs (Fig. S2, ESI†) have an increase in off-current (I_{OFF}).

However, the most striking observation is the improvement in μ, with maximum μ (μ_{MAX}) $\geq$ 1 cm^2 V^{-1} s^{-1} with all n-type dopants. Fig. 2b and Fig. S3 (ESI†) give a statistical overview of the impact of n-doping on O-IDTBR mobility, where the saturation value of μ is extracted from the $I_D^{0.5}$ *vs.* V_G plots,[18,27] taken from at least 13 devices per system that were fabricated simultaneously; there are clear differences in performance variation, with O-IDTBR:N-DMBI exhibiting notably narrower electron mobility distribution. We also note the differences between the EPR peak signal intensity and transistor performance characteristics, specifically I_{OFF} and μ trends. For example, DMBI-BDZC has the smallest EPR signal yet the biggest change in I_{OFF}, relative to the other materials. Similarly, TBAF gives the highest EPR signal but the lowest improvement in μ. However, these observations are strictly qualitative in nature, and additional, supportive characterisation studies would be required to provide a quantitative description of doping efficiency. Although the transistor and EPR samples were prepared in the same way, these differences arise because the transistor measurements are on solid-state thin-films, whereas the EPR samples are in the solution-phase, with different solubility and phase separation (see the Experimental section for more details). Despite these differences, we note that the overall measured transistor mobility values are the highest reported to-date for NFAs,[17] and amongst the highest reported for solution-processed n-type small-molecules.[18]

Given the nature of the OTFT structure used here, and the role of access resistance in top-gate, bottom-contact OTFTs, another point to consider when discussing μ changes, is the impact from thin-film thickness and its role on contact resistance (R_C). Specifically, a thicker film typically results in a higher R_C magnitude *via* access resistance from the carriers travelling between the source and the channel. Here, all the layers (*i.e.* pristine and doped systems) have the same thickness ($\approx$100 nm). As such, the layer thickness is not expected to be detrimental for both μ and system-to-system device performance, as it remains constant. We do note, however, that doping is widely renowned for impacting R_C by reducing the width of the Schottky barrier at the semiconductor/metal interface. We therefore expect that there will be a change in R_C due to

Open Access Article. Published on 10 March 2021. Downloaded on 8/24/2022 2:34:21 PM.
This article is licensed under a Creative Commons Attribution-NonCommercial 3.0 Unported Licence.

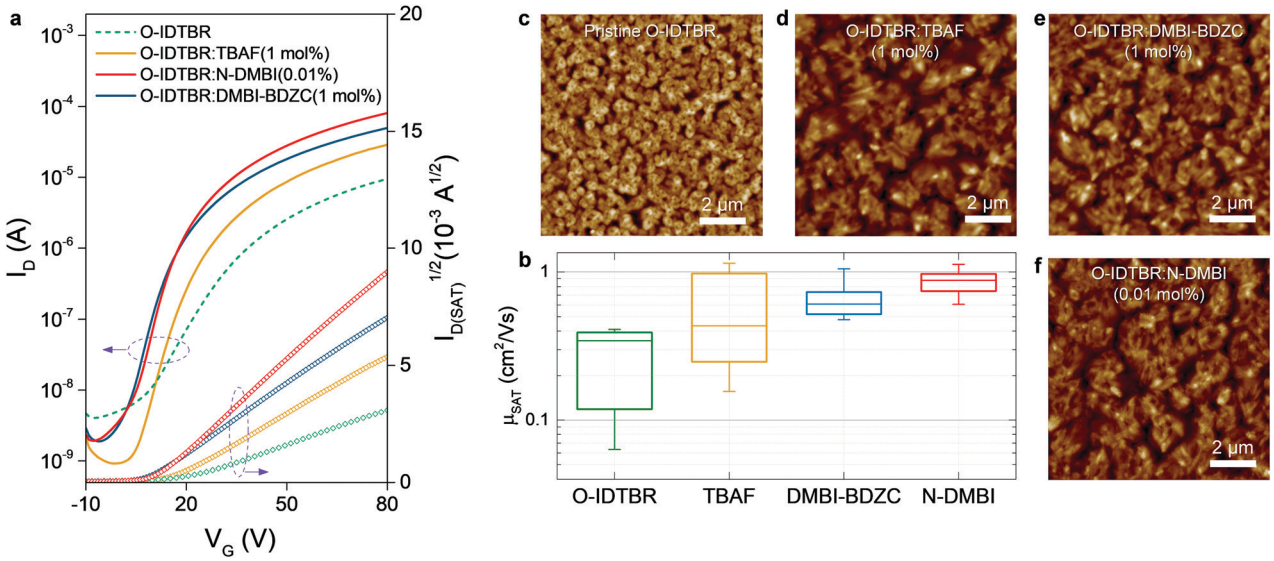

Fig. 2 (a) Representative transfer characteristics for the best-performing n-doped O-IDTBR systems, as compared to pristine O-IDTBR OTFTs. All transistors have 50 and 1000 μm channel length and width, respectively. We note that relative IOFF is higher in pristine O-IDTBR from gate leakage from an unpatterned semiconductor and leaky dielectric, with the current set of devices displayed because they were fabricated in a controlled manner *i.e.* at the same time, with I_{OFF} behaviour shown in Fig. S2 (ESI†). (b) Saturation mobility statistics for pristine and best-performing systems, extracted from $\sqrt{I_{D_SAT}}$ *vs.* V_G. Statistics are taken over at least 13 devices each. AFM topography images for (c) pristine O-IDTBR and the best-performing n-doped systems: (d) O-IDTBR:TBAF (1 mol%), (e) O-IDTBR:DMBI-BDZC (1 mol%) and (f) O-IDTBR:N-DMBI (0.01 mol%).

doping, and this will be part of the overall μ performance enhancement that we see for the various doped systems.[5]

Trap analysis. Another characteristic change that happens in transistors upon doping is a reduction in threshold voltage (V_T). We observe this here in the best-performing n-doped transistors, compared to pristine O-IDTBR, and it is representative of donated charge carriers filling pre-existing trap states.[26,28,29] This reduction in V_T, along with the clear improvement in subthreshold slope (SS) in the doped devices, can be attributed to improvement in interfacial charge trapping[26] and semiconductor structural disorder.[30] To understand the trap filling effect further, we probed how the density of states changes with n-doping – as opposed to introduction of free carriers in the LUMO – by calculating the trap densities for both pristine and best-performing n-doped systems (Table 2). First we used SS to estimate the density of traps at the semiconductor/dielectric interface (D_{tr}^{SS}) using:[31]

$$D_{tr}^{SS} = \frac{C_i}{e^2}\left(\frac{eSS}{k_B T \ln(10)} - 1\right) \quad (1)$$

where k_B is the Boltzmann constant and T the temperature. D_{tr}^{SS} is representative of shallow trap states closest to the LUMO. We find that D_{tr}^{SS} is twice larger for OTFTs based on pristine O-IDTBR (2.2×10^{12}), as compared to the best-performing doped systems, which each have similar values (1×10^{12}, 9.8×10^{11} and 1×10^{12} in TBAF (1 mol%), N-DMBI (0.01 mol%) and DMBI-BDZC (1 mol%), respectively). We then used a second method to estimate the interfacial trap density (N_{tr}) from V_T and onset voltages (V_{on})

$$N_{tr} = \frac{C_i|V_T - V_{on}|}{e} \quad (2)$$

where C_i is the areal capacitance of the dielectric layer and e is the elementary charge. N_{tr} is representative of deep trap states furthest from the LUMO. Similar to D_{tr}^{SS}, we find that N_{tr} in pristine O-IDTBR is greater than twice that in the best-performing doped systems, with $N_{tr} = 2.8 \times 10^{11}$, compared to 1.2×10^{11}, 1.9×10^{11} and 1.3×10^{11} in TBAF (1 mol%), N-DMBI (0.01 mol%) and DMBI-BDZC (1 mol%), respectively. Although the values for D_{tr}^{SS} and N_{tr} are different, which is representative of their physical nature and the energies of the trap states (shallow/deep), we see the same trend in both: the calculated D_{tr}^{SS} and N_{tr} values indicate that there is a

Table 1 The influence of n-doping on key OTFT parameters: V_T, μ_{SAT_MAX}, μ_{SAT_AVG} at best-performing concentrations, and I_{OFF} at highly doped concentrations

	OTFT parameters			
Materials system	V_T (V)	$I_{OFF_10\,mol\%}$ (A)	μ_{SAT_MAX} (cm^2 V^{-1} s^{-1})	μ_{SAT_AVG} (cm^2 V^{-1} s^{-1})
O-IDTBR	18.8	0.76×10^{-9}	0.4	0.3
O-IDTBR:TBAF	14.7	4.4×10^{-9}	1.1	0.4
O-IDTBR:N-DMBI	10.8	0.75×10^{-9}	1.1	0.9
O-IDTBR:DMBI-BDZC	7.6	5.7×10^{-9}	1.0	0.6

Table 2 Trap densities corresponding to representative devices in Fig. 2a, where dielectric capacitance, C_i, is 1.7×10^{-9} F cm^{-2}

	Trap density and transistor parameters			
Materials System	SS (V dec^{-1})	D_{tr}^{SS} (cm^{-2} eV^{-1})	V_T–V_{ON} (V)	N_{tr} (cm^{-2})
O-IDTBR	12.2	2.2×10^{12}	26.7	2.8×10^{11}
O-IDTBR:TBAF	6.0	1.0×10^{12}	11.5	1.2×10^{11}
O-IDTBR:N-DMBI	5.5	9.8×10^{11}	17.8	1.9×10^{11}
O-IDTBR:DMBI-BDZC	5.9	1.0×10^{12}	12.5	1.3×10^{11}

Open Access Article. Published on 10 March 2021. Downloaded on 8/24/2022 2:34:21 PM.
This article is licensed under a Creative Commons Attribution-NonCommercial 3.0 Unported Licence.

marked improvement in trap states between the pristine O-IDTBR and the three n-doped systems, where each of the doped systems then has a similar density of traps close to the Fermi level.[32,33] This suggests that each type of dopant has filled pre-existing O-IDTBR trap states to a similar extent. Given that the best-performing systems each exhibit different average and statistical μ variation, this in-turn suggests that doping is not solely responsible for the measured μ or increase in μ as compared to the pristine O-IDTBR. We also note here that such trap-filling may also be useful in other NFA-based devices where trapping affects carrier extraction and recombination.[34,35]

Morphology

If doping is not solely responsible for the changes in measured μ, and therefore carrier concentration, conductivity and charge transport, another possible influence is the dopant impact on morphology. The latter phenomenon either inadvertently arises from the physical presence of the dopant changing OSC packing motif,[5,6] or, as shown recently, underlying doping mechanisms impacting crystallisation and growth of the solid-state layer.[2,10,11,36] Although these two points are extremely difficult to disentangle, the former is especially prominent in small-molecule OTFTs and typically known to inhibit charge transport, whilst the latter may be influential given the sensitivity of NFA μ/performance to chemical structure variation.[17] We therefore used atomic force microscopy (AFM) to investigate the surface morphology of pristine, best-performing and highly doped thin-films. Fig. 2c–f and Fig. S4a–c (ESI†) show stark differences in all films, with grain size and surface roughness (Fig. S4d, ESI†) depending on both n-dopant type and concentration. Each optimally doped semiconductor layer shows an extended, more uniform morphology/microstructure, as compared to the pristine O-IDTBR layer. The improved extension and uniformity of the crystals correlate with larger crystallites and subsequently a lower density of grain boundaries. The latter grain boundary density across the transistor channel is known to impact both mobility and device performance, with the grain boundaries acting as trapping sites, directly inhibiting charge transport.[37] Such effects are indeed expected to contribute to the μ improvement in the case of n-doped O-IDTBR OTFTs, as well as towards reduction in trap densities, as shown in the D_{tr}^{SS} and N_{tr} calculations. Along with dopant-induced free electrons filling pre-existing trap states, the morphology changes, and the relationship between layer uniformity and grain boundary density, are expected to contribute towards the lower trap densities observed in all optimally doped O-IDTBR layers.

Grazing incidence wide-angle X-ray scattering. To explore the differences observed with AFM in more detail, we used grazing incidence wide-angle X-ray scattering (GIWAXS) (Fig. 3). Remarkably, we detect the presence of a new structural orientation perpendicular to the substrate, namely the [020] orientation, which appears to correlate with OTFT high electron mobility characteristics. We also detect another orientation, [110] – previously associated with a typical O-IDTBR packing motif[38] – with two signature peaks located at q = 0.61 Å^{-1} in the q_z direction and q = 0.43 Å^{-1} at an angle of 40° from the horizon, respectively (Fig. 3a and Fig. S5a, e, ESI†). We find that the [110] orientation is the only orientation detectable in layers that exhibit the lowest electron mobility, *i.e.* pristine and TBAF (10 mol%). On the other hand, the [020] orientation appears

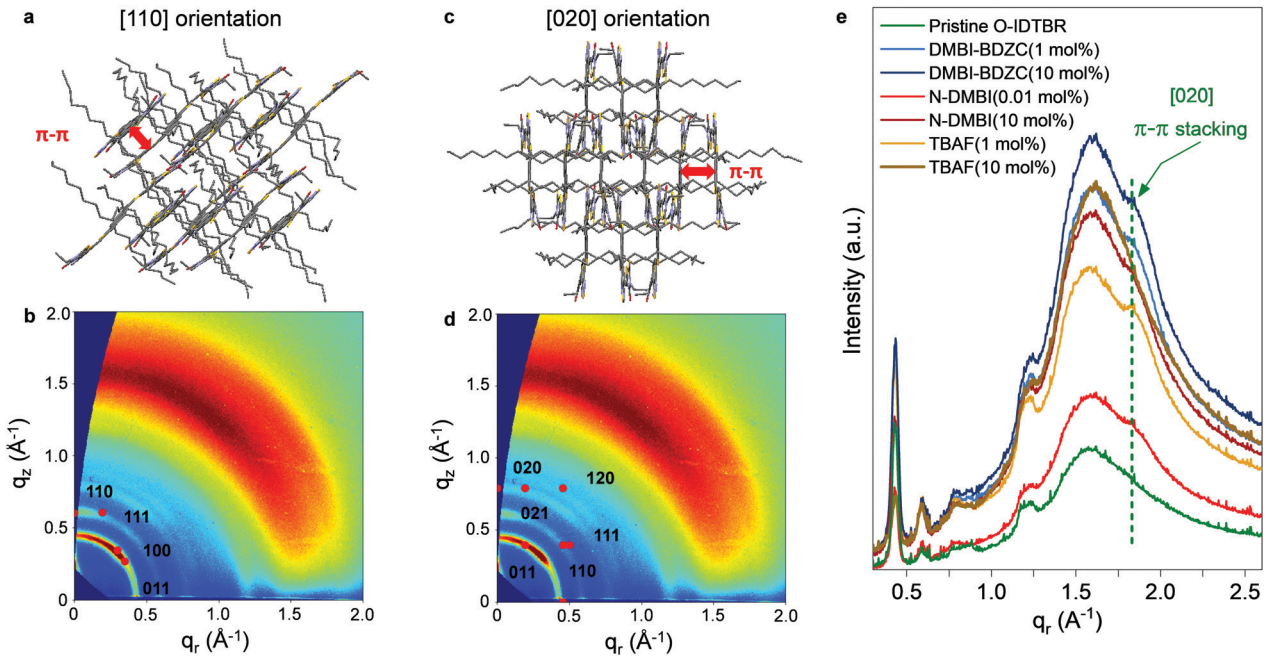

Fig. 3 Representative [110] and [020] indexing shown for the mixed-orientation 0.01 mol% N-DMBI thin-film, which produced the best-performing OTFTs overall, including [110] orientation with tilted π–π stacking (a) schematic and (b) indexing and [020] orientation with in-plane π–π stacking (c) schematic and (d) indexing. (e) Integrated plots of GIWAXS patterns along the q_r direction (in-plane) for pristine and n-doped films. The latter shows in-plane π-stacking only occurs with the mixed [110] and [020] orientations.

Open Access Article. Published on 10 March 2021. Downloaded on 8/24/2022 2:34:21 PM.
This article is licensed under a Creative Commons Attribution-NonCommercial 3.0 Unported Licence.

alongside [110] in all other, higher mobility layers (Fig. S5, ESI†). Fig. 3a and b show representative indexing of both orientations in best-performing system, N-DMBI (0.01 mol%). The integrated GIWAXS patterns (Fig. 3e) find in-plane π-stacking in mixed orientation films, suggesting [020] has preferred in-plane π-stacking (see Fig. 3a and b). The latter may benefit charge transport parallel to the substrate in OTFTs and introduce higher μ compared to [110].

Further evidence of this trend comes from the fact that the fraction of [020] appears to correlates with OTFT μ. To quantify the relative intensity of the two orientations, we calculated the fraction of each orientation across the entire film, from the intensity of the corresponding peaks in q_z-direction.[39] The results are shown in Fig. S6 and Table S2 (ESI†). We find that, for example, 0.01% N-DMBI contains more [020] than 10 mol% N-DMBI which corresponds to a higher μ. We note here that the fact TBAF(10 mol%) does not exhibit the [020] orientation is unexpected, especially considering its presence in TBAF (1 mol%). This is likely because, at 10 mol%, the system is overloaded beyond the optimum doping concentration, which removes beneficial effects on crystallisation and growth. We also note that the ratio between [110] and [020] appears to be dependent on the type and/or amount of dopant; however, it is difficult to give a quantitative ratio between the two orientations. One experimental approach to investigate these effects further is to study sequential doping *via* solvent annealing or through sublimation, to first form the thin-film, and then doping to investigate the development of the [020] orientation, when provides with enough thermal energy. However, such focused investigations are beyond the scope of this work.

Theory

Density functional theory. The evidence so-far suggests doping and morphology-changes are synergistically responsible for the improvement in O-IDTBR charge transport and electron mobility. To shed some light on the underlying TBAF, N-DMBI and DMBI-BDZC doping mechanism(s), we first used density functional theory (DFT) calculations. We find that DMBI-BDZC supports integer charge transfer from O-IDTBR, with E_{HOMO} of diazocine (−3.82 eV) slightly higher than experimental E_{LUMO} of O-IDTBR (−3.90 eV) (Fig. 4a).[40–43] On the other hand, for TBAF doping, DFT supports the formation of an adduct by chemical reaction *via* the nucleophilic addition of the fluoride anion to the thioketone. The resulting adduct can then undergo an electron transfer to an adjacent O-IDTBR molecule, similar to the mechanism previously proposed by Katz *et al.* (Fig. 4b).[12,20] We note here that all samples were processed and measured under inert conditions and therefore the TBAF is not hydrated; heating/annealing hydrated TBAF can cause it to decompose into the hydrogen difluoride salt, which may lead to different doping mechanisms than those described here. Finally, we find that N-DMBI only acts as an n-dopant when it loses an H-atom and transfers a hydrogen anion to the O-IDTBR (Fig. 4c), following the hydride transfer mechanism described previously.[21,44] However, we do note that, although the findings in our DFT results are substantiated throughout the literature, there are more recent, spectroscopic findings that exclude hydride transfer as a doping mechanism for N-DMBI-based systems, and rather support mechanisms of electron transfer between an electron acceptor and a donor.[45] Overall, the DFT results show the three dopants appear to n-dope the O-IDTBR *via* different mechanisms, with each dopant altering the electronic structure of O-IDTBR differently.[2,10,11] Thus it is reasonable to hypothesise that the different interactions lead to the structural differences observed, though this is currently extremely difficult to disentangle/demonstrate experimentally.

One particular question raised by these results is: how can DMBI-BDZC, TBAF and N-DMBI n-dope O-IDTBR *via* different mechanisms, yet result in the same new structural orientation?

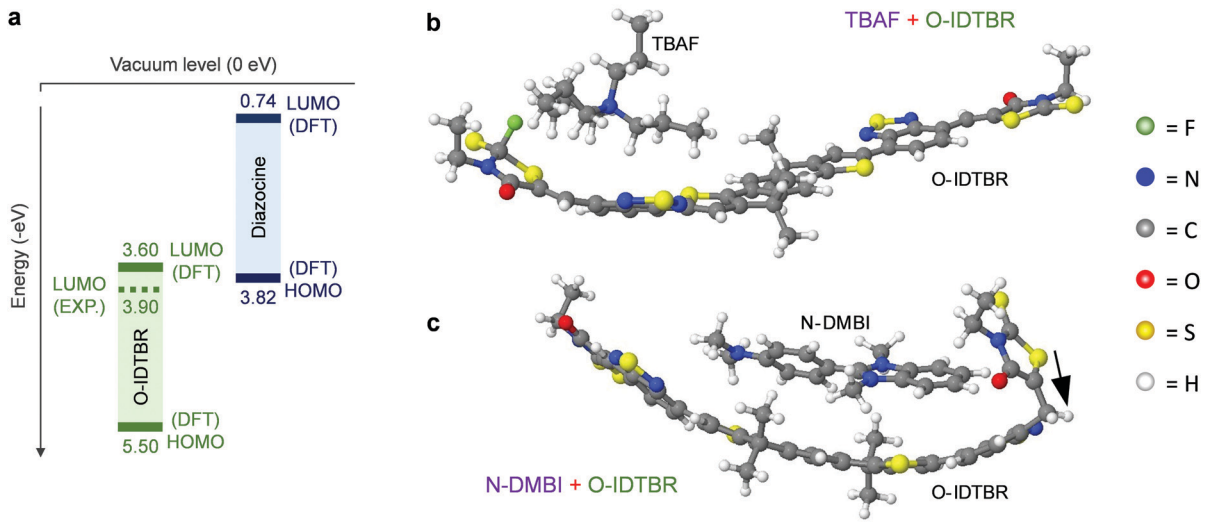

Fig. 4 (a) Energy level diagram for integer charge transfer doping of O-IDTBR by DMBI-BDZC. (b) TBAF complex with an O-IDTBR molecule in a configuration where the F-atom is chemisorbed onto a C-atom in the O-IDTBR. (c) N-DMBI complex with an O-IDTBR molecule in a configuration where the H-atom has been transferred from N-DMBI to O-IDTBR, as shown with the black arrow.

Open Access Article. Published on 10 March 2021. Downloaded on 8/24/2022 2:34:21 PM.
This article is licensed under a Creative Commons Attribution-NonCommercial 3.0 Unported Licence.

For DMBI-BDZC and N-DMBI, the fact that they are from the same family may result in a specific interaction between their functional unit and the O-IDTBR. Although this is extremely difficult to explore with atomic-level DFT calculations, we investigated possible configurations for N-DMBI- and DMBI-BDZC-doped O-IDTBR. We find that, in the case of N-DMBI-doped O-IDTBR, *i.e.* an O-IDTBR molecule with an H^- anion attached (Fig. S7, ESI†), there are a number of possible configurations with comparable energies. This leads to the possibility of various effects on crystal morphology and orientation. For DMBI-BDZC, *i.e.* a diazocine complex with an O-IDTBR molecule (Fig. S8, ESI†), the O-IDTBR molecule retains a more or less flat configuration, akin to those found for certain structures with N-DMBI (Fig. S7, ESI†). This shows that, although doping mechanisms are different with N-DMBI and DMBI-BDZC, the ensuing structure for the O-ITDBR (or a number of possible such structures) can be similar in the different cases. We find that this is the same for TBAF, *i.e.* an O-IDTBR molecule with an F^- anion attached (Fig. S9, ESI†) in terms of possible configurations with comparable energies. Overall if different O-IDTBR end configurations have comparable energies, the presence DMBI-BDZC, N-DMBI or TBAF could therefore have similar effects on O-IDTBR in terms of crystal morphology and orientation. The final structure depends on the complex details of dopant–host interactions, including complex steric constraints, which are not fully taken into account in small-scale DFT calculations. The similar effects that different dopants can have on morphology is part of a broader, important message from this work, which is the first to highlight such dopant-induced structure–property relationship.

The results outlined in this work suggest that different n-dopants – that rely on different doping mechanisms – lead to similar morphological changes. This raises a poignant question on the origin of the morphology changes and the exact role of the dopant. Possible reasons include, but are not limited to: (i) changes in the packing motif of the host OSC[5,6] upon interaction with the dopant during layer deposition; (ii) interactions between neutral and charged molecules while in solution; (iii) space-filling effects;[46] and (iv) charge-transfer processes.[47] Overall, further understanding of this complex topic and mechanisms governing molecular doping of OSCs, would certainly require further focused research.

Molecular dynamics, kinetic Monte Carlo simulations. Next, we used a combination of molecular dynamics, polarizable force-fields and kinetic Monte Carlo simulations to investigate the impact of O-IDTBR typical [110] and new [020] orientations, on both μ_e and hole μ (μ_h) mobilities.[48,49] Fig. 5a shows the results. We find the mobility tensor, $\hat{\boldsymbol{\mu}}$, is highly anisotropic (*circa* 1 : 1 : 10), with the largest component found along the z-axis for both [110] and [020] (Fig. 5b). The latter favors charge transport along the substrate/channel plane. The [020] crystal orientation corresponds to π–π stacking along the substrate, whilst [110] is tilted by ≈45° with respect to the substrate. To account for these differences, $\hat{\boldsymbol{\mu}}$ was averaged in the substrate plane (see ESI†), leading to calculated values μ_e = 0.22 $cm^2\ V^{-1}\ s^{-1}$ and = 0.29 $cm^2\ V^{-1}\ s^{-1}$ for [110] and [020],

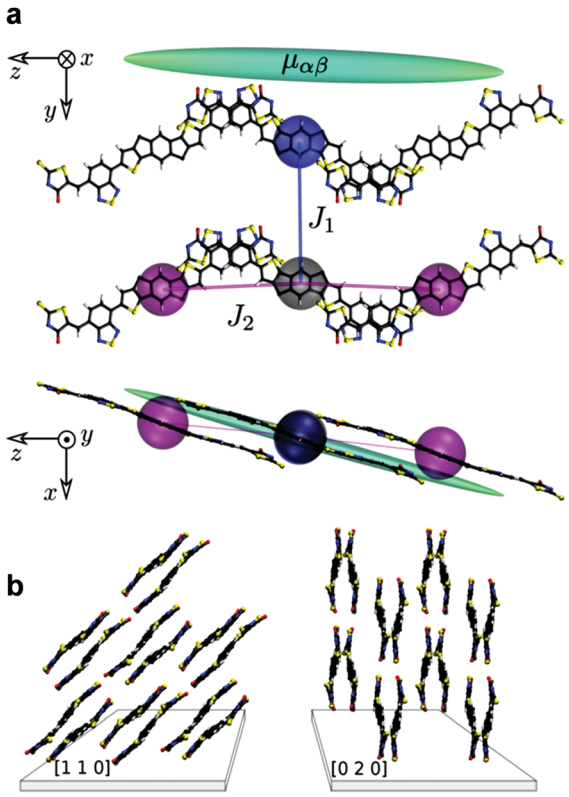

Fig. 5 (a) Packing of O-IDTBR (side chains are omitted) with spheres showing the geometrical centers of molecules. Lines show charge hopping directions, with electronic couplings $J_2 \sim 2J_1$. Mobility tensor $\hat{\boldsymbol{\mu}}$ is visualized by an ellipsoid and is very anisotropic due to orientation of the preferential orientation of long molecular axes along the z-direction. (b) The [110] and [020] orientations of the unit cell with respect to the substrate.

respectively. Although μ is ≈25% greater in [020], the similarity suggests the experimentally measured μ values are more likely due to more uniform molecular alignment in the OTFT channel (due to the anisotropic mobility tensor), or from dopant-induced, less defective domain boundaries, and hence shallower trap states in the density of states. The latter can result directly from either doping mechanisms, or morphology enhancements. Interestingly, we also find that μ_h is similar to μ_e, with μ_h = 0.06 $cm^2\ V^{-1}\ s^{-1}$ and = 0.08 $cm^2\ V^{-1}\ s^{-1}$ for [110] and [020], respectively. This finding suggests reasonably balanced, intrinsic ambipolar transport in O-IDTBR, in line with its relatively large electron affinity and relatively small ionization energy.[50,51] In this study, such ambipolar transport is not observed since the OTFTs are engineered to operate as n-channel devices. Specifically, we have used silver source/drain electrodes coated with a polyethyleneimine (PEIE) injection layer which raises their work function making them ideal for selective electron injection in the LUMO. However, these theoretical results highlight the possibility of p-type doping as a route to enhance μ_h to match the high μ_e reported here. Such high ambipolar mobility would be useful for the implementation of complementary logic circuits comprising a single OSC (albeit spatially doped) as the active layer, and will be the subject of further studies.

Open Access Article. Published on 10 March 2021. Downloaded on 8/24/2022 2:34:21 PM.
This article is licensed under a Creative Commons Attribution-NonCommercial 3.0 Unported Licence.

Experimental

Organic semiconductor preparation

The dopant solutions, as well as the stock O-IDTBR solution, were prepared in chlorobenzene. Doping concentrations were calculated as molar percentages (mol%) of the total O-IDTBR molar mass. The dopant solutions were admixed with the O-IDTBR solution for the various doping concentrations, such that the overall dopant:O-IDTBR solution concentration is always 10 mg mL^{-1}. All dopant:O-IDTBR solutions were stirred overnight at 50 °C prior to the transistor fabrication.

Thin-film transistor fabrication and measurements

Top-gate, bottom-contact devices were fabricated on 18 × 18 mm glass substrates cleaned using acetone and IPA, before 15 minutes of UV–ozone treatment. The clean substrates were transferred into an N_2-glove box for the remaining transistor fabrication and measurements. 30 nm Ag source-drain contacts were deposited *via* thermal evaporation through a shadow mask. An initial layer of PEIE (0.04% polyethleneimine in methoxyethanol) was spin-coated at 5000 rpm for 60 s and thermally annealed at 70 °C for 5 minutes. The dopant:O-IDTBR solutions were then spin-coated from warm (70 °C) solutions at 1000 rpm for 30 s, and thermally annealed at 120 °C for 5 minutes, after which the hot-plate was switched off, allowing the devices to gradually cool to room temperature (≈23 °C). A CYTOP dielectric later was then spin-coated at 2000 rpm for 60 seconds to produce a 900 nm thick film, which was annealed at 50 °C for 80 minutes. Finally, a 40 nm Al gate electrode was thermally evaporated through a shadow mask. A Keysight B2912A Precision Source/Measure Unit was used to measure the transistor current–voltage characteristics.

Electron paramagnetic resonance

A continuous wave Bruker EMX PLUS spectrometer was used to record the EPR spectra at low temperatures (5 K) using a liquid helium setup, as well as a standard resonator for high sensitivity. The spectra were recorded using 0.625 mW of microwave power with 5 G modulation amplitude and 100 kHz modulation frequency. We have chosen to investigate samples in the solution state, instead of the solid state, for practical purposes related to the accurate positioning of the material in the EPR tube.

Atomic force microscopy

Atomic force microscopy (AFM) images were acquired using an Agilent 5500 in tapping mode. Gwyddion was used for image analysis and processing.

Grazing-incident wide-angle X-ray scattering

GIWAXS was data was gathered using the 11-BM Complex Materials Scattering (CMS) beamline of the National Synchrotron Light Source II (NSLS-II), Brookhaven National Laboratory. The semiconductor layers were prepared following the same processing steps used for the fabrication of field-effect transistors. The samples were then illuminated using X-rays with a wavelength of 0.0918 nm, at an incident angle of 0.10°. An in-vacuum CCD (Photonic Science) detector – calibrated by silver behenate and located 227 mm away from the thin-film samples – was tilted at ≈19° from the incident X-ray beam direction. To minimize the air scattering, measurements were performed under vacuum at an exposure time of 100 seconds. To gain a better resolution in q-space and limit the X-ray footprint on the sample, the thin films were partially removed to maintain only ∼5 mm length along the X-ray direction. The data analysis was performed by a custom-made program, SciAnalysis, including integrated plots along Q_r and Q_z directions, as well as the overall patterns.

Density functional theory (DFT) calculations

The code NWCHEM[52] and B3LYP[53,54] exchange–correlation functional were used to perform DFT calculations. The 6-31G* or 6-311G* Gaussian basis sets were typically used to perform structure relaxation. van der Waals interactions were included with the DFT-D3 method.[55] The reported DFT HOMO and LUMO energy values utilized the more complete 6-311+G* basis.

Computer simulations of charge transport in crystalline O-IDTBR

The initial cell parameters and atomic positions were taken by analysing the X-ray scattering patterns and equilibrated in the *NPT* ensemble, before evaluating the electronic coupling elements,[56] reorganization and site energies.[57] The corresponding master equation, with one molecule representing one hopping site, and Markus charge transfer rates were solved using the kinetic Monte Carlo (MC) algorithm. The hole and electron mobilities were evaluated directly from the MC trajectories. All simulations were performed using the GROMACS[58,59] and VOTCA-CTP packages,[49] where further details are provided in the ESI.†

Conclusions

In summary, we employed several different molecular n-type dopants, namely DMBI-BDZC, TBAF and N-DMBI, in transistors made from the prototypical small-molecule O-IDTBR. Under optimal n-doping, we found that all dopant molecules enhanced electron mobility to greater than 1 cm^2 V^{-1} s^{-1}. Analysis of the organic semiconductor using EPR and field-effect measurements show that n-type doping plays a role in the observed electron transport and the measured mobility improvements. Morphology and microstructure analysis by AFM and GIWAXS techniques, on the other hand, revealed that the dopant molecules also behave as morphology-modifiers, and lead to a new, dopant-induced O-IDTBR structural orientation, namely [020]. Theoretical calculations support the idea that the synergistic effects of n-type doping and minute microstructure alterations, are responsible for the improved electron transport, whilst highlighting O-IDTBR as an intrinsically ambipolar material with balanced hole and electron mobilities. By reporting record high NFA mobilities from the simple admixing of molecular dopants and O-IDTBR, we identify beneficial interactions between the dopant and host that result in a dopant-induced packing orientation underpinning previously unreported mechanisms.

Open Access Article. Published on 10 March 2021. Downloaded on 8/24/2022 2:34:21 PM.
This article is licensed under a Creative Commons Attribution-NonCommercial 3.0 Unported Licence.

We investigate this, for the first time, by combining the GIWAXS analysis, single crystal microstructure and molecular modelling to provide a theoretical understanding of the origin of improved electron transport and mobility. Overall, this work demonstrates n-type doping as a powerful technique for improving charge carrier transport in solution-processed n-type small-molecules: the finding that electron transport improves *via* the coexistence of trap filling and morphology-changes, both establishes and probes a bigger picture relevant to a broad range of organic semiconducting devices – from transistors to photovoltaics,[60] – for the development of high-performance organic electronics.

Conflicts of interest

There are no conflicts to declare.

Acknowledgements

The authors acknowledge the King Abdullah University of Science and Technology (KAUST) for financial support. LT acknowledges the use of the GRNET HPC facility ARIS under project STEM-2. This research used CMS beamline of the National Synchrotron Light Source II, a U.S. Department of Energy (DOE) Office of Science User Facility operated for the DOE Office of Science by Brookhaven National Laboratory under Contract No. DE-SC0012704. DA received funding from the BMBF grants InterPhase and MESOMERIE (FKZ 13N13661, FKZ 13N13656) and the European Union Horizon 2020 research and innovation program "Widening materials models" under Grant Agreement No. 646259 (MOSTOPHOS). D. A. also acknowledges KAUST for hosting his sabbatical. A. M. acknowledges postdoctoral support of the Alexander von Humboldt Foundation.

Notes and references

1 B. Lussem, M. Riede and K. Leo, *Doping of organic semiconductors*, 2013.
2 I. E. Jacobs and A. J. Moulé, *Adv. Mater.*, 2017, **29**, 1703063.
3 Y. Xu, H. Sun, A. Liu, H.-H. Zhu, W. Li, Y.-F. Lin and Y.-Y. Noh, *Adv. Mater.*, 2018, **30**, 1801830.
4 M. Waldrip, O. D. Jurchescu, D. J. Gundlach and E. G. Bittle, *Adv. Funct. Mater.*, 2020, **30**, 1904576.
5 A. F. Paterson, Y.-H. Lin, A. D. Mottram, Z. Fei, M. R. Niazi, A. R. Kirmani, A. Amassian, O. Solomeshch, N. Tessler, M. Heeney and T. D. Anthopoulos, *Adv. Electron. Mater.*, 2017, **4**, 1700464.
6 B. Lüssem, C.-M. Keum, D. Kasemann, B. Naab, Z. Bao and K. Leo, *Chem. Rev.*, 2016, **116**, 13714–13751.
7 I. Salzmann, G. Heimel, M. Oehzelt, S. Winkler and N. Koch, *Acc. Chem. Res.*, 2016, **49**, 370–378.
8 H. Mendez, G. Heimel, A. Opitz, K. Sauer, P. Barkowski, M. Oehzelt, J. Soeda, T. Okamoto, J. Takeya, J.-B. Arlin, J.-Y. Balandier, Y. Geerts, N. Koch and I. Salzmann, *Angew. Chem., Int. Ed.*, 2013, **52**, 7751–7755.
9 B. Lüssem, M. Riede and K. Leo, *Phys. Status Solidi A*, 2013, **210**, 9–43.
10 A. F. Paterson, L. Tsetseris, R. Li, A. Basu, H. Faber, A.-H. Emwas, J. Panidi, Z. Fei, M. R. Niazi, D. H. Anjum, M. Heeney and T. D. Anthopoulos, *Adv. Mater.*, 2019, **31**, 1900871.
11 J. Panidi, A. F. Paterson, D. Khim, Z. Fei, Y. Han, L. Tsetseris, G. Vourlias, P. A. Patsalas, M. Heeney and T. D. Anthopoulos, *Adv. Sci.*, 2018, **5**, 1700290.
12 Y. Han, Z. Fei, Y.-H. Lin, J. Martin, F. Tuna, T. D. Anthopoulos and M. Heeney, *npj Flexible Electron.*, 2018, **2**, 11.
13 J. Panidi, J. Kainth, A. F. Paterson, S. Wang, L. Tsetseris, A.-H. Emwas, M. A. McLachlan, M. Heeney and T. D. Anthopoulos, *Adv. Funct. Mater.*, 2019, **29**, 1902784.
14 P. Wei, J. H. Oh, G. Dong and Z. Bao, *J. Am. Chem. Soc.*, 2010, **132**, 8852–8853.
15 J. Yuan, Y. Zhang, L. Zhou, G. Zhang, H.-L. Yip, T.-K. Lau, X. Lu, C. Zhu, H. Peng, P. A. Johnson, M. Leclerc, Y. Cao, J. Ulanski, Y. Li and Y. Zou, *Joule*, 2019, **3**, 908–909.
16 A. Wadsworth, M. Moser, A. Marks, M. S. Little, N. Gasparini, C. J. Brabec, D. Baran and I. McCulloch, *Chem. Soc. Rev.*, 2019, **48**, 1596–1625.
17 H. Bristow, K. J. Thorley, A. J. P. White, A. Wadsworth, M. Babics, Z. Hamid, W. Zhang, A. F. Paterson, J. Kosco, J. Panidi, T. D. Anthopoulos and I. McCulloch, *Adv. Electron. Mater.*, 2019, **5**, 1900344.
18 A. F. Paterson, S. Singh, K. J. Fallon, T. Hodsden, Y. Han, B. C. Schroeder, H. Bronstein, M. Heeney, I. McCulloch and T. D. Anthopoulos, *Adv. Mater.*, 2018, **30**, 1801079.
19 J. Kim, D. Khim, K.-J. Baeg, W.-T. Park, S.-H. Lee, M. Kang, Y.-Y. Noh and D.-Y. Kim, *Adv. Funct. Mater.*, 2016, **26**, 7886–7894.
20 X. Zhao, D. Madan, Y. Cheng, J. Zhou, H. Li, S. M. Thon, A. E. Bragg, M. E. DeCoster, P. E. Hopkins and H. E. Katz, *Adv. Mater.*, 2017, **29**, 1606928.
21 S. P. Schießl, H. Faber, Y.-H. Lin, S. Rossbauer, Q. Wang, K. Zhao, A. Amassian, J. Zaumseil and T. D. Anthopoulos, *Adv. Mater.*, 2016, **28**, 3952–3959.
22 S. Rossbauer, C. Muller and T. D. Anthopoulos, *Adv. Funct. Mater.*, 2014, **24**, 7116–7124.
23 C. W. Koh, J. H. Heo, M. A. Uddin, Y. W. Kwon, D. H. Choi, S. H. Im and H. Y. Woo, *ACS Appl. Mater. Interfaces*, 2017, **9**, 43846–43854.
24 J. Luo, J. Xia, H. Yang, L. Chen, Z. Wan, F. Han, H. A. Malik, X. Zhu and C. Jia, *Energy Environ. Sci.*, 2018, **11**, 2035–2045.
25 D. Kiefer, A. Giovannitti, H. Sun, T. Biskup, A. Hofmann, M. Koopmans, C. Cendra, S. Weber, L. J. Anton Koster, E. Olsson, J. Rivnay, S. Fabiano, I. McCulloch and C. Müller, *ACS Energy Lett.*, 2018, **3**, 278–285.
26 A. Salleo, *Organic Electronics*, Wiley-VCH Verlag GmbH & Co. KGaA, 2013, pp. 341–380, DOI: 10.1002/9783527650965.ch14.
27 H. H. Choi, K. Cho, C. D. Frisbie, H. Sirringhaus and V. Podzorov, *Nat. Mater.*, 2018, **17**, 2–7.
28 J. H. Kim, S. W. Yun, B.-K. An, Y. D. Han, S.-J. Yoon, J. Joo and S. Y. Park, *Adv. Mater.*, 2013, **25**, 719–724.

 This journal is © The Royal Society of Chemistry 2021

Open Access Article. Published on 10 March 2021. Downloaded on 8/24/2022 2:34:21 PM.
This article is licensed under a Creative Commons Attribution-NonCommercial 3.0 Unported Licence.

29 A. Salleo, *Mater. Today*, 2007, **10**, 38–45.
30 C. Liu, G. Li, R. Di Pietro, J. Huang, Y.-Y. Noh, X. Liu and T. Minari, *Phys. Rev. Appl.*, 2017, **8**, 034020.
31 S. M. Sze, *Physics of Semiconductor Devices*, John Wiley & Sons, Wiley Eastern Limited, New Delhi, India, 1981.
32 W. L. Kalb and B. Batlogg, *Phys. Rev. B: Condens. Matter Mater. Phys.*, 2010, **81**, 035327.
33 A. F. Paterson, A. D. Mottram, H. Faber, M. R. Niazi, Z. Fei, M. Heeney and T. D. Anthopoulos, *Adv. Electron. Mater.*, 2019, **5**, 1800723.
34 N. Gasparini, M. Salvador, T. Heumueller, M. Richter, A. Classen, S. Shrestha, G. J. Matt, S. Holliday, S. Strohm, H.-J. Egelhaaf, A. Wadsworth, D. Baran, I. McCulloch and C. J. Brabec, *Adv. Energy Mater.*, 2017, **7**, 1701561.
35 C. G. Shuttle, N. D. Treat, J. D. Douglas, J. M. J. Fréchet and M. L. Chabinyc, *Adv. Energy Mater.*, 2012, **2**, 111–119.
36 Y. Han, C. Jianya, Z. Ke, T. Yabing, M. Xiangyi, X. Xianbin and M. Wei, *Adv. Energy Mater.*, 2018, **0**, 1703672.
37 K. V. Nguyen, M. M. Payne, J. E. Anthony, J. H. Lee, E. Song, B. Kang, K. Cho and W. H. Lee, *Sci. Rep.*, 2016, **6**, 33224.
38 S. Holliday, R. S. Ashraf, A. Wadsworth, D. Baran, S. A. Yousaf, C. B. Nielsen, C.-H. Tan, S. D. Dimitrov, Z. Shang, N. Gasparini, M. Alamoudi, F. Laquai, C. J. Brabec, A. Salleo, J. R. Durrant and I. McCulloch, *Nat. Commun.*, 2016, **7**, 11585.
39 J. W. Ward, R. Li, A. Obaid, M. M. Payne, D.-M. Smilgies, J. E. Anthony, A. Amassian and O. D. Jurchescu, *Adv. Funct. Mater.*, 2014, **24**, 5052–5058.
40 D. Baran, T. Kirchartz, S. Wheeler, S. Dimitrov, M. Abdelsamie, J. Gorman, R. S. Ashraf, S. Holliday, A. Wadsworth, N. Gasparini, P. Kaienburg, H. Yan, A. Amassian, C. J. Brabec, J. R. Durrant and I. McCulloch, *Energy Environ. Sci.*, 2016, **9**, 3783–3793.
41 H. Cha, J. Wu, A. Wadsworth, J. Nagitta, S. Limbu, S. Pont, Z. Li, J. Searle, M. F. Wyatt, D. Baran, J.-S. Kim, I. McCulloch and J. R. Durrant, *Adv. Mater.*, 2017, **29**, 1701156.
42 D. Baran, R. S. Ashraf, D. A. Hanifi, M. Abdelsamie, N. Gasparini, J. A. Röhr, S. Holliday, A. Wadsworth, S. Lockett, M. Neophytou, C. J. M. Emmott, J. Nelson, C. J. Brabec, A. Amassian, A. Salleo, T. Kirchartz, J. R. Durrant and I. McCulloch, *Nat. Mater.*, 2017, **16**, 363–369.
43 R.-Z. Liang, M. Babics, V. Savikhin, W. Zhang, V. M. Le Corre, S. Lopatin, Z. Kan, Y. Firdaus, S. Liu, I. McCulloch, M. F. Toney and P. M. Beaujuge, *Adv. Energy Mater.*, 2018, **8**, 1800264.
44 B. D. Naab, S. Guo, S. Olthof, E. G. B. Evans, P. Wei, G. L. Millhauser, A. Kahn, S. Barlow, S. R. Marder and Z. Bao, *J. Am. Chem. Soc.*, 2013, **135**, 15018–15025.
45 I. Denti, S. Cimò, L. Brambilla, A. Milani, C. Bertarelli, M. Tommasini and C. Castiglioni, *Chem. Mater.*, 2019, **31**, 6726–6739.
46 R. Yu, H. Yao, Z. Chen, J. Xin, L. Hong, Y. Xu, Y. Zu, W. Ma and J. Hou, *Adv. Mater.*, 2019, **31**, 1900477.
47 P. Y. Yee, D. T. Scholes, B. J. Schwartz and S. H. Tolbert, *J. Phys. Chem. Lett.*, 2019, **10**, 4929–4934.
48 C. Poelking and D. Andrienko, *J. Chem. Theory Comput.*, 2016, **12**, 4516–4523.
49 V. Rühle, A. Lukyanov, F. May, M. Schrader, T. Vehoff, J. Kirkpatrick, B. Baumeier and D. Andrienko, *J. Chem. Theory Comput.*, 2011, **7**, 3335–3345.
50 N. B. Kotadiya, A. Mondal, P. W. M. Blom, D. Andrienko and G.-J. A. H. Wetzelaer, *Nat. Mater.*, 2019, **18**, 1182–1186.
51 D. Abbaszadeh, A. Kunz, N. B. Kotadiya, A. Mondal, D. Andrienko, J. J. Michels, G.-J. A. H. Wetzelaer and P. W. M. Blom, *Chem. Mater.*, 2019, **31**, 6380–6386.
52 M. Valiev, E. J. Bylaska, N. Govind, K. Kowalski, T. P. Straatsma, H. J. J. V. Dam, D. Wang, J. Nieplocha, E. Aprá, T. L. Windus and W. A. de Jong, *Comput. Phys. Commun.*, 2010, **181**, 1477–1489.
53 A. D. Becke, *J. Chem. Phys.*, 1993, **98**, 5648–5652.
54 P. J. Stephens, F. J. Devlin, C. F. Chabalowski and M. J. Frisch, *J. Phys. Chem.*, 1994, **98**, 11623–11627.
55 S. Grimme, J. Antony, S. Ehrlich and H. Krieg, *J. Chem. Phys.*, 2010, **132**, 154104.
56 B. Baumeier, J. Kirkpatrick and D. Andrienko, *Phys. Chem. Chem. Phys.*, 2010, **12**, 11103–11113.
57 C. Poelking, E. Cho, A. Malafeev, V. Ivanov, K. Kremer, C. Risko, J.-L. Brédas and D. Andrienko, *J. Phys. Chem. C*, 2013, **117**, 1633–1640.
58 B. Hess, C. Kutzner, D. van der Spoel and E. Lindahl, *J. Chem. Theory Comput.*, 2008, **4**, 435–447.
59 B. Hess, D. van der Spoel, E. Lindahl, J. C. Smith, M. R. Shirts, P. Bjelkmar, P. Larsson, P. M. Kasson, R. Schulz, R. Apostolov, S. Pronk and S. Páll, *Bioinformatics*, 2013, **29**, 845–854.
60 Y. Lin, Y. Firdaus, M. I. Nugraha, F. Liu, S. Karuthedath, A.-H. Emwas, W. Zhang, A. Seitkhan, M. Neophytou, H. Faber, E. Yengel, I. McCulloch, L. Tsetseris, F. Laquai and T. D. Anthopoulos, *Adv. Sci.*, 2020, **7**, 1903419.